PAPER

Insights into the enhancement of oxygen evolution catalysis in Ce-mediated amorphous CoFe-based (oxy)hydroxides

Ji-Dong Song,†[a] Hao Hu,†[b] Jian-Li Mi, [ID] *[a] Fu-Ming Qi,[a] Bei-Bei Xiao [ID] [c] and Zhi-Zhong Yuan*[a]

Heteroatom doping and nanostructure engineering are recognized as pivotal strategies for enhancing the oxygen evolution reaction (OER) performance of layered double hydroxides (LDHs) and (oxy)hydroxides. However, the reason for performance improvement remains controversial. Herein, we report Ce-incorporated amorphous CoFe-(oxy)hydroxide nanoparticles on nickel foam (NF) *via* a one-step electrodeposition method, achieving excellent OER activity with a low overpotential (η = 0.220 V at 10 mA cm^{-2} in 1.0 M KOH), ranking among the top-performing CoFe-based OER catalysts. Intriguingly, despite the fact that Ce incorporation can reduce the overpotential of CoFe-(oxy)hydroxide, the intrinsic activity and the reaction kinetics are suppressed through Ce incorporation. Instead, the enhancement of OER activity primarily stems from the small particle size and the fast charge transfer. Ce incorporation suppresses the particle coalescence during synthesis, thereby increasing the electrochemically active surface area. In addition, Ce incorporation modulates the interfacial charge-transfer resistance effectively. This work highlights a method for designing high-performance OER catalysts through morphological engineering and electric conductivity modulation.

1. Introduction

Electrochemical water splitting has emerged as one of the most promising hydrogen production technologies for generating high-purity hydrogen without any other byproducts.[1,2] While the cathodic hydrogen evolution reaction (HER) demonstrates relatively fast kinetics, the anodic oxygen evolution reaction (OER) suffers from inherent kinetic limitations due to its multi-step proton-coupled electron transfer process.[3] Although noble metal oxides (*e.g.*, RuO$_2$ and IrO$_2$) are benchmark OER electrocatalysts, their industrial scalability is constrained by their scarcity and high cost.[4,5] Up to now, substantial research endeavors have been devoted to designing cost-effective alternatives, particularly transition metal-based catalysts.[6–10]

CoFe layered double hydroxides (CoFe-LDHs) are widely recognized as promising electrocatalysts for the OER.[11–14] Unfortunately, the intrinsically low electrical conductivity and the limited number of exposed active sites are the primary issues for LDHs.[15,16] Several strategies have been developed to enhance the electrocatalytic OER performance of LDH-based electrocatalysts. One effective approach involves integrating LDHs with conductive substrates, such as nickel foam (NF)[17] and carbon-based materials,[18,19] thereby improving the electron transfer. Additionally, construction of nanostructured materials to increase the specific surface area has been proven to be a reliable strategy to maximize the active site exposure. For instance, liquid exfoliation has been employed to synthesize single-layer LDHs, which significantly enhance the OER activity compared to their bulk counterparts.[20] Recent advancements highlight heteroatom doping and heterostructure engineering as powerful strategies for optimizing LDH-based electrocatalysts.[21] Heteroatom incorporation can modulate the electron distribution of adjacent atoms, thereby boosting catalytic performance. For instance, Wang *et al.* prepared Ce-doped CoFe-LDHs on NF *via* a hydrothermal method, which achieved exceptional OER activity due to the lattice distortion and defect formation within the LDH host layers.[22] Similarly, heterostructure construction induces interfacial charge redistribution, further improving OER performance. Chen *et al.* demonstrated a hierarchical Co$_3$O$_4$@CoFe-LDH heterostructure on carbon cloth, achieving an ultralow overpotential of 0.237 V at 10 mA cm^{-2} for the OER.[23] Moreover,

[a]School of Materials Science and Engineering, Jiangsu University, Zhenjiang 212013, China. E-mail: jlmi@ujs.edu.cn, yzzjs@ujs.edu.cn
[b]School of Chemical and Pharmaceutical Engineering, Changzhou Vocational Institute of Engineering, Changzhou, 213164, China
[c]School of Energy and Power Engineering, Jiangsu University of Science and Technology, Zhenjiang 212003, China
† These authors contributed equally to this work.

amorphous (oxy)hydroxides, with their unique short-range ordered atomic configurations, abundant defects, and high-density active sites, offer synergistic advantages for OER enhancement.[24,25] Li *et al.* developed a hybrid electrocatalyst combining amorphous NiCo-LDH with 3D $NiCo_2O_4$ nanowire arrays on NF, resulting in outstanding performance in overall water electrolysis.[25]

Despite significant interest in the heteroatom doping and heterostructure engineering of CoFe-based LDHs, identifying the precise cause of performance improvement remains challenging, as it stems from the combined effects of multiple factors. For instance, doping is often accompanied by changes in morphology and size, which are frequently overlooked. Ce, as a critical rare earth element, has a unique 4f electronic structure and good electrical conductivity, offering a great opportunity for modulating the electronic structure to enhance the OER activity. For example, Wu *et al.* prepared Ce-doped NiFe LDHs on NF by hydrothermal synthesis with excellent OER performance, owing to the reversible redox between Ce^{3+} and Ce^{4+} states.[26] Herein, we synthesized amorphous Ce-doped CoFe-(oxy)hydroxides directly on NF *via* a one-step electrodeposition method. The resulting Ce-doped CoFe-(oxy)hydroxides exhibit enhanced OER activity, requiring an overpotential of only 0.220 V to achieve 10 mA cm^{-2} in 1.0 M KOH. Crucially, we observed that Ce incorporation suppresses particle growth, thereby enlarging the electrochemically active surface area (ECSA). Meanwhile, Ce incorporation modulates the interfacial charge transfer kinetics efficiently. The improved OER performance arises primarily from the increased ECSA and optimized interfacial charge transfer kinetics.

2. Results and discussion

Ce-incorporated CoFe-(oxy)hydroxides deposited on NF were synthesized *via* electrodeposition using metal salts (Co(NO$_3$)$_2$·6H$_2$O, Fe(NO$_3$)$_3$·9H$_2$O, and Ce(NO$_3$)$_3$·6H$_2$O) in molar ratios of Co : Fe : Ce = 1 : 1 : x (x = 0.2, 0.4, 0.6, 0.8), and the final products were designated as CoFeCe$_x$ (see details in the SI). For comparison, Ce-free CoFe-(oxy)hydroxide (labeled as CoFe) was prepared under identical conditions without Ce(NO$_3$)$_3$·6H$_2$O. Fig. 1a–e and Fig. S1 present the scanning electron microscopy (SEM) images of CoFe and Ce-incorporated variants (CoFeCe$_x$) on NF substrates. Particle aggregates are distributed on the NF substrates in all samples. Compared to Ce-free CoFe, a decrease in average particle size occurs in CoFeCe$_x$. The results demonstrate that Ce incorporation modulates the growth kinetics of CoFe-(oxy)hydroxide particles, thereby effectively suppressing particle agglomeration. The decrease in the average grain size upon Ce incorporation can be ascribed to the dopant element's role as a microstructural stabilizer for fine particles, and a similar phenomenon was observed in Ce-doped ZnO nanoparticles.[27] The small particle sizes not only provide the enhanced exposed active sites but also correlate with the improved electrolyte accessibility. Such

nanoscale refinement provides a structural basis for the enhanced OER activity observed in subsequent electrochemical characterization. Energy dispersive spectroscopy (EDS) analysis (Fig. S2) verified the successful incorporation of cerium into CoFeCe$_x$, and the Ce content was found to increase roughly with x, as anticipated.

Transmission electron microscopy (TEM) and high-resolution transmission electron microscopy (HRTEM) were employed to further identify the detailed structure of CoFeCe$_{0.4}$. Fig. 2a and b present the TEM and HRTEM images of an ultrasonically exfoliated fragment from the CoFeCe$_{0.4}$ electrode, revealing a featureless morphology devoid of lattice fringes. The amorphous nature of CoFeCe$_{0.4}$ is further corroborated by the diffuse ring pattern observed in the selected area electron diffraction (SAED) (Fig. 2c). In addition, X-ray diffraction (XRD) patterns (Fig. S3) reveal only the intense diffraction peaks corresponding to metallic Ni originating from the NF substrates for both CoFe and CoFeCe$_{0.4}$, further confirming the amorphous structures of the electrodeposited CoFe-(oxy)hydroxide and Ce-incorporated CoFe-(oxy)hydroxide particles. The Raman spectrum of CoFe (Fig. 1f) exhibits three representative bands: the bands at 453 and 525 cm^{-1} are, respectively, assigned to the e$_g$ bending and a$_{1g}$ stretching modes of the Co–O bonds, while the peak at 685 cm^{-1} is attributed to the Fe–O vibrational modes in CoFe-(oxy)hydroxide.[28,29] The results confirm the formation of amorphous CoFe-(oxy)hydroxide. The amorphous structure of Ce-incorporated CoFe-(oxy)hydroxides may further improve the OER performance due to the unique short-range ordered atomic configurations, abundant defects, and high-density active sites. Elemental mapping images (Fig. 2d) confirm the homogeneous distribution of Fe, Co, Ce and O elements throughout the CoFeCe$_{0.4}$ fragment. The uniform Ce dispersion implies atomic-level integration into the CoFe matrix rather than secondary phase formation.

The surface composition and oxidation states of CoFeCe$_{0.4}$ were analyzed using X-ray photoelectron spectroscopy (XPS) and compared with CoFe. As shown in the XPS survey spectra (Fig. 3a), CoFe exhibited characteristic signals of C, O, Fe, Co, and Ni, while CoFeCe$_{0.4}$ exhibited additional Ce signatures alongside C, O, Fe, and Co. A molar ratio of Co : Fe : Ce = 1 : 1.77 : 0.59 is obtained for CoFeCe$_{0.4}$ from the XPS analysis (Table S1). The discrepancy between XPS and EDS results may primarily stem from the fact that XPS is a surface-sensitive analytical technique. Detailed analysis of the high-resolution O 1s spectra (Fig. 3b) revealed three distinct oxygen species: lattice oxygen (M–O bonds, ~529.3 eV), hydroxyl (–OH, ~530.9 eV), and weakly absorbed H$_2$O molecules (~532.1 eV for CoFe and ~532.3 eV for CoFeCe$_{0.4}$).[30] The proportion of lattice oxygen in the O 1s spectrum increases from 10% for CoFe to 16% for CoFeCe$_{0.4}$, suggesting enhanced structural oxygen content upon Ce incorporation. In the Fe 2p spectra (Fig. 3c), the prominent peaks at 711.8 eV (Fe 2p$_{3/2}$) and 725.3 eV (Fe 2p$_{1/2}$) are consistent with Fe^{3+} in FeOOH, confirming that Fe predominantly adopts the +3 oxidation state in both CoFe and CoFeCe$_{0.4}$.[31] For the Co 2p spectra (Fig. 3d), the characteristic peaks of CoFe at 781.2 eV (Co 2p$_{3/2}$) and 796.9 eV (Co 2p$_{1/2}$)
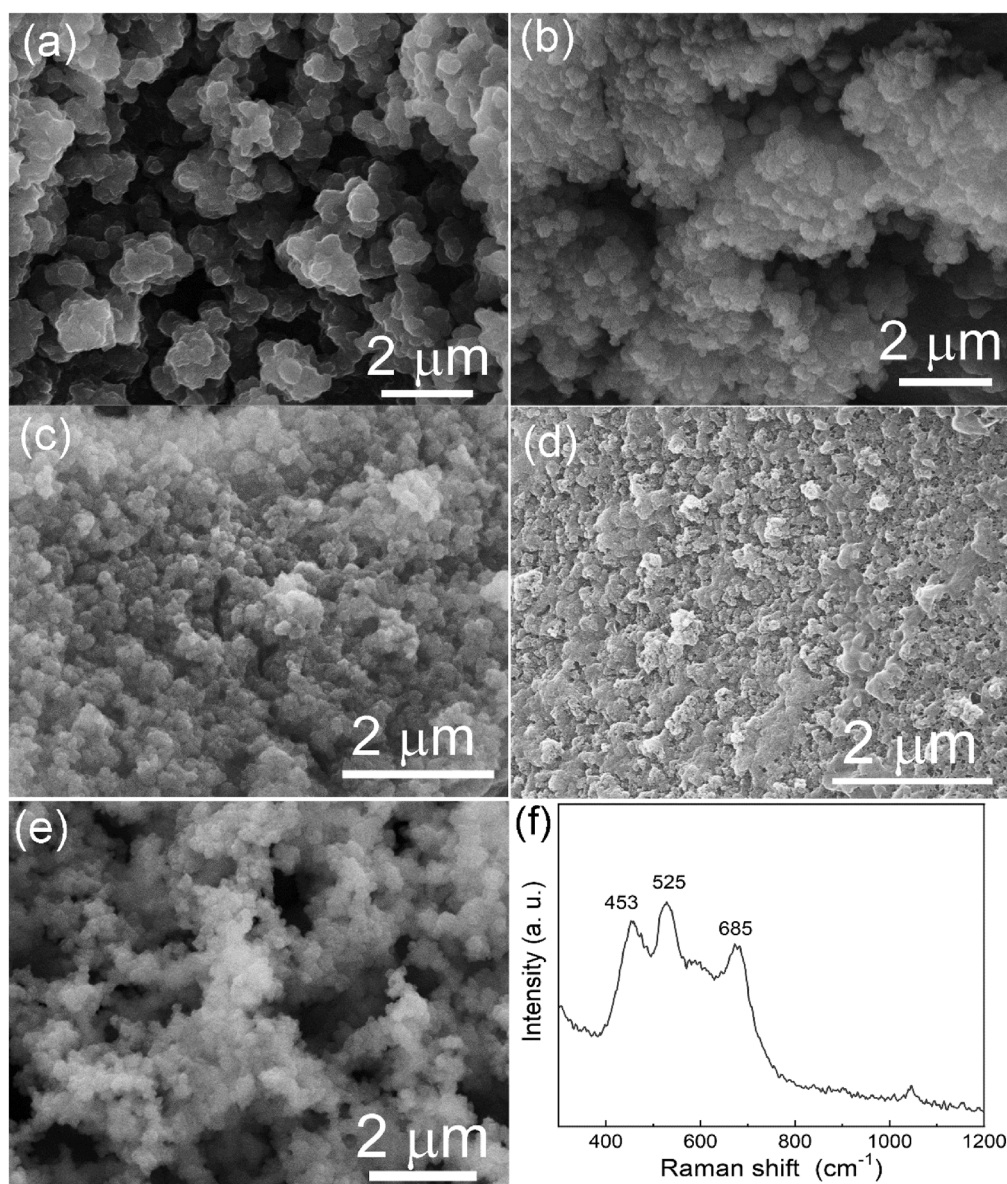
Fig. 1 SEM images of (a) CoFe, (b) $CoFeCe_{0.2}$, (c) $CoFeCe_{0.4}$, (d) $CoFeCe_{0.6}$, and (e) $CoFeCe_{0.8}$. (f) Raman spectrum of CoFe.

align with Co^{2+} of $Co(OH)_2$, indicating that Co primarily exists as Co^{2+}.[32] Notably, these peaks undergo a slight shift to higher binding energies in $CoFeCe_{0.4}$, which implies electron density redistribution around Co centers induced by Ce incorporation. The Ni 2p spectra (Fig. 3e) reveal similar features for both CoFe and $CoFeCe_{0.4}$, with contributions from metallic Ni, NiO, and Ni^{2+} in $Ni(OH)_2$. While Ni and NiO originate from the NF substrate, the Ni^{2+} are likely incorporated into the CoFe and $CoFeCe_{0.4}$ particles during electrodeposition.[33] No significant binding energy shifts are observed for Ni species, suggesting minimal electronic interaction between Ni and Ce. Finally, the Ce 3d spectrum of $CoFeCe_{0.4}$ (Fig. 3f) was deconvoluted into spin–orbit doublets, where u and v refer to the $3d_{3/2}$ and $3d_{5/2}$ spin–orbit components, respectively. The fitting results indicate dominant Ce^{4+} states (labeled v, v^{II}, v^{III}, u, u^{II}, and u^{III})

alongside Ce^{3+} species (labeled v^{I} and u^{I}). The coexistence of Ce^{4+} and Ce^{3+} is indicative of the formation of oxygen vacancies introduced by Ce incorporation. Collectively, these results demonstrate that Ce incorporation induces only minor electronic perturbations to Co in $CoFeCe_{0.4}$, with the primary oxidation states of Fe^{3+} and Ni^{2+} remaining almost unchanged.

The electrocatalytic OER performance of the CoFe and $CoFeCe_x$ (x = 0.2, 0.4, 0.6, and 0.8) series as well as the bare NF electrode was systematically evaluated in 1 M KOH. Fig. 4a shows the linear sweep voltammetry (LSV) curves (iR-corrected) recorded at 5 mV s^{-1} after activation, and Fig. 4b exhibits the overpotentials (η) required to achieve the current density of 10 and 50 mA cm^{-2}. NF exhibits relatively poor activity, requiring an overpotential of 0.361 V to reach 10 mA cm^{-2}. The η required to reach 10 mA cm^{-2} decreases from η = 0.251 V for
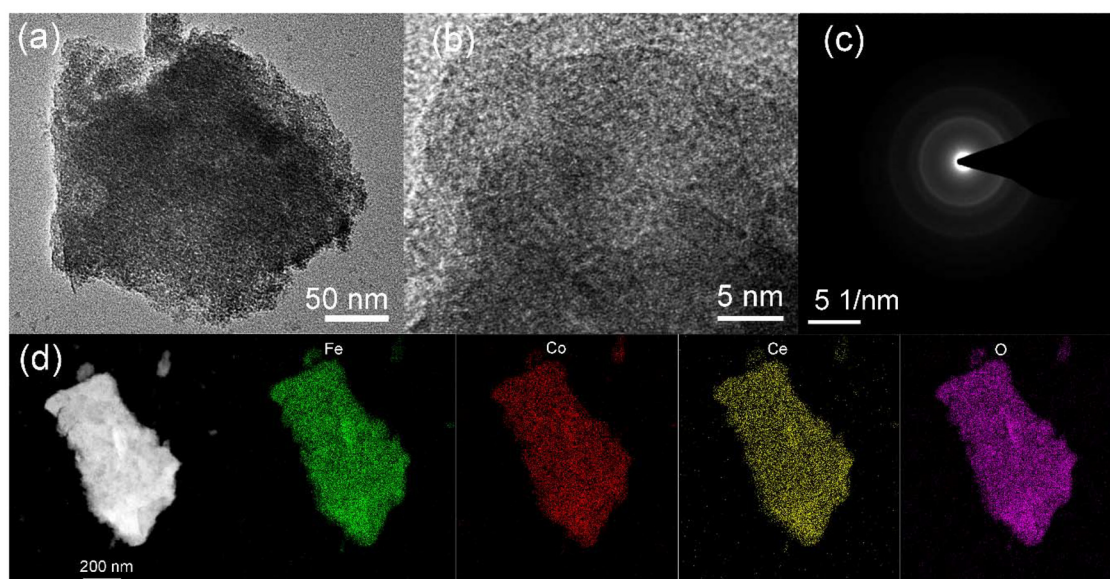
Fig. 2 (a) TEM image, (b) HRTEM image, (c) SAED pattern, and (d) elemental mapping images of CoFeCe$_{0.4}$.

CoFe to 0.237, 0.220, 0.223, and 0.227 V for CoFeCe$_{0.2}$, CoFeCe$_{0.4}$, CoFeCe$_{0.6}$, and CoFeCe$_{0.8}$, respectively, demonstrating that Ce incorporation can further reduce the overpotential of CoFe-(oxy)hydroxide. The OER activity of CoFe in this work is close to the reported value for CoFe-LDH.[34] Notably, CoFeCe$_{0.4}$ exhibits optimal activity with η = 0.220 V at 10 mA cm^{-2} and η = 0.262 V at 50 mA cm^{-2}, and the OER activity of CoFeCe$_{0.4}$ is among the most advanced CoFe-based OER catalysts and better than the noble metal-based RuO$_2$ and IrO$_2$ catalysts (Table S2). Kinetic analysis through Tafel slopes (Fig. 4c) provides further insight into the OER performance. Fitting the linear regions of the Tafel plots to the Tafel equation (η = $b \log j + a$, where j is the current density and b is the Tafel slope) yields progressively increasing slopes of 42.1, 47.6, 58.0, 62.1, and 67.7 mV dec^{-1} for CoFe, CoFeCe$_{0.2}$, CoFeCe$_{0.4}$, CoFeCe$_{0.6}$, and CoFeCe$_{0.8}$, respectively. The typical CV curve of CoFeCe$_{0.4}$ is shown in Fig. S4. There is a peak pair in the potential range of 1.25–1.40 V of the CV curve that originates from the redox couple of Ni^{2+}/Ni^{3+}.[35] We also derived the Tafel slopes of CoFeCe$_{0.4}$ from the forward and backward branches of the CV curve, finding a slightly smaller slope value from the backward branch due to the effect of the oxidative peak. The inverse correlation between the Ce content and OER kinetics indicates that higher Ce contents compromise reaction dynamics despite the improvement of overpotentials, likely due to the lower intrinsic activity of the Ce-based active centers.[12] Chronopotentiometry curves at a static current density of 10 mA cm^{-2} (Fig. 4d) further confirm that the CoFeCe$_{0.4}$ exhibits the lowest overpotential. The observed decoupling between improved overpotential and deteriorated kinetics suggests that Ce-induced improvements of the OER may originate from extrinsic factors such as increased active sites or improved conductivity rather than intrinsic catalytic activity enhancement.

To elucidate the enhanced OER activity of CoFeCe$_x$, we measured the electrochemical double-layer capacitance (C_{dl}) *via* cyclic voltammetry (CV) within the non-faradaic region at varying sweep rates (Fig. S5). The C_{dl} value increases with the increase of Ce content, reaching the maximum value for CoFeCe$_{0.8}$, which indicates that Ce incorporation increases the number of active sites. However, since both the electric double layer and adsorption pseudocapacitance contribute to the total capacitance, deriving C_{dl} from CV may introduce inaccuracies. Therefore, we systematically analyzed the charge transfer kinetics and ECSA through electrochemical impedance spectroscopy (EIS) at 1.6 V (*vs.* RHE).[36] Nyquist plots of CoFe and CoFeCe$_x$ (Fig. 4e) were fitted using the Watzele and Bandarenka equivalent circuit (inset, Fig. 4e),[37] where R_u represents the uncompensated electrolyte resistance, R_{ct} corresponds to charge transfer resistance, and R_a relates to the resistance of the adsorption of OER intermediates. CPE$_{dl}$ and CPE$_a$ describe the constant phase element (CPE) related to the responses of the electric double layer and adsorption pseudocapacitance, respectively. The adsorption capacitance (C_a) was calculated using $C_a = R_a^{-1} \cdot (R_a \cdot Y_0)^{1/\alpha}$, where Y_0 and the exponent α are the parameters for CPE$_a$.[36] ECSA values were derived by normalizing C_a with a specific unit area capacitance (C_s) of 0.3 mF cm^{-2}. Table 1 exhibits the R_u, R_{ct}, C_a, and ECSA values of different catalysts. Firstly, R_{ct} follows a volcano trend with the Ce content, reaching a minimum (0.118 Ω) for CoFeCe$_{0.4}$, indicating optimal interfacial charge transfer efficiency. Secondly, ECSA values increase dramatically from 101.3 cm^2 for CoFe to over 1000 cm^2 for Ce-incorporated catalysts, and CoFeCe$_{0.6}$ has the largest ECSA (1356.8 cm^2), which may be attributed to the Ce-induced suppression of particle growth during synthesis. Both the improved charge transfer capability and the enhanced active site exposure result in the superior OER performance of
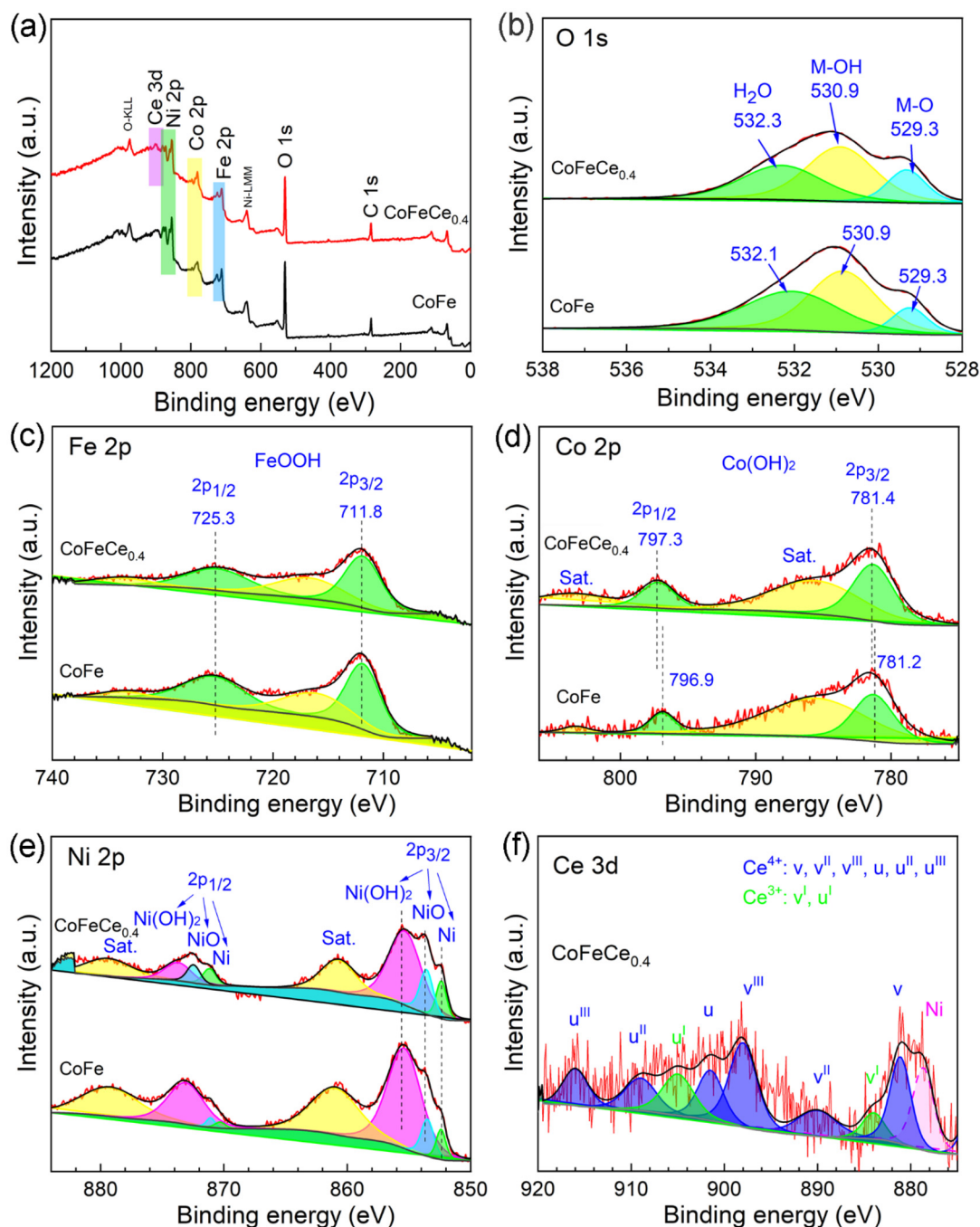
Fig. 3 XPS spectra of CoFe and CoFeCe$_{0.4}$. (a) Surveys, (b) O 1s, (c) Fe 2p, (d) Co 2p, (e) Ni 2p, and (f) Ce 3d.

CoFeCe$_{0.4}$. For the bare NF electrode, the Nyquist plot is well-fitted by a simple equivalent circuit excluding adsorption pseudocapacitance (Fig. S6), indicating limited active sites in NF.

The intrinsic OER activity of the catalysts was evaluated through ECSA-normalized current density analysis (Fig. 4f), revealing distinct trends in catalytic performance. The overpotentials at 0.1 mA cm$^{-2}_{\mathrm{ECSA}}$ follow an ascending order of CoFe (0.247 V) < CoFeCe$_{0.4}$ (0.258 V) < CoFeCe$_{0.1}$ (0.263 V) <

CoFeCe$_{0.8}$ (0.274 V) < CoFeCe$_{0.6}$ (0.276 V). The results demonstrate that CoFe exhibits the highest intrinsic OER activity. Despite the electron redistribution in CoFeCe$_x$ as evidenced by the XPS, CoFe shows better intrinsic activity than CoFeCe$_x$. It has been reported that motifs such as Co–Co and Co–Fe serve as the primary reaction sites in CoFe systems.[38] As Ni is incorporated into CoFe and CoFeCe$_x$, Ni also plays an important role in enhancing OER performance.[39] Furthermore, Ce cations may function as additional
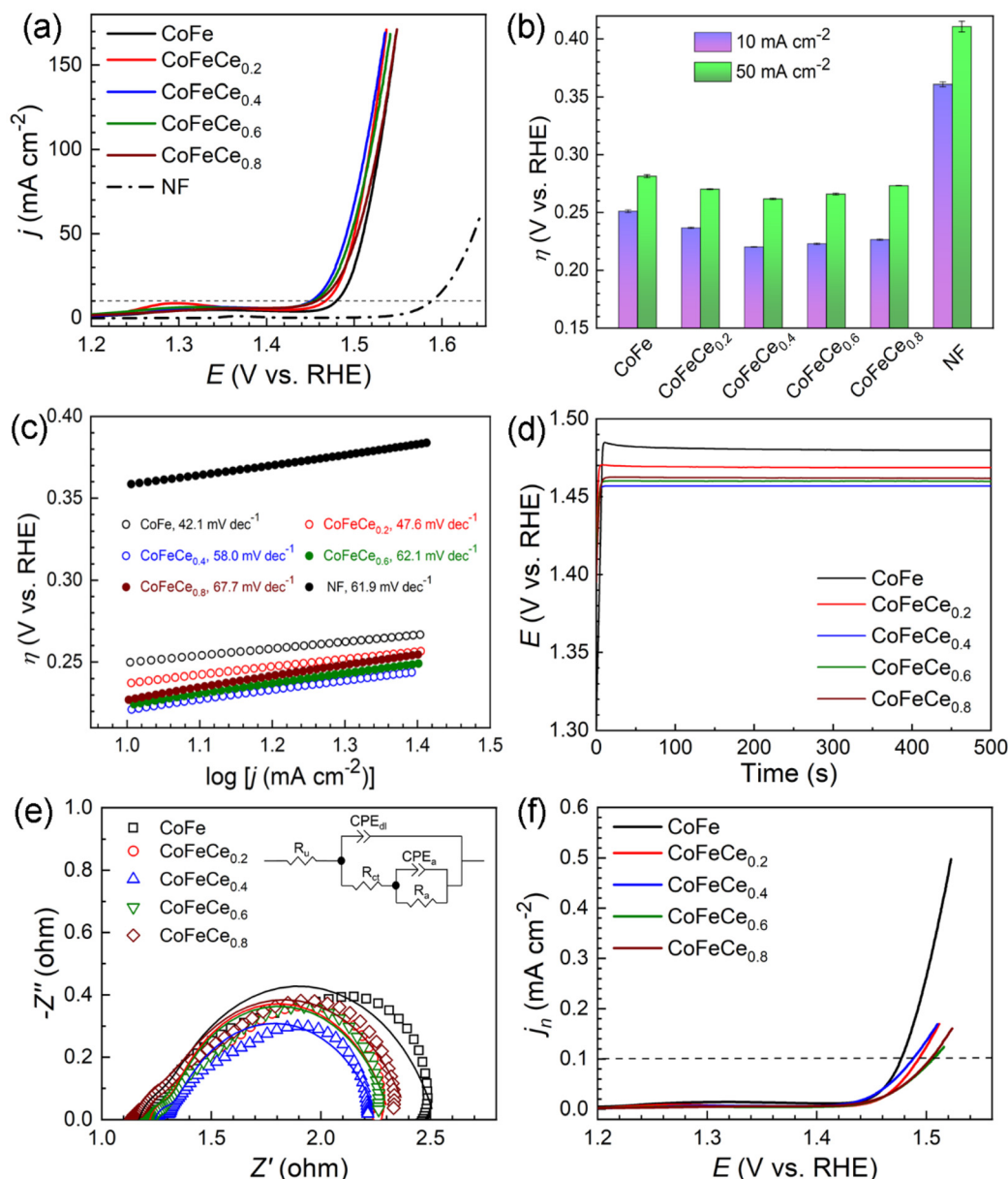
Fig. 4 (a) LSV curves of CoFe and CoFeCe$_x$ (x = 0.2, 0.4, 0.6, 0.8). (b) Overpotentials (η) to achieve current densities of 10 and 50 mA cm^{-2}. (c) Tafel plots. (d) Chronopotentiometry curves at a static current density of 10 mA cm^{-2}. (e) EIS plots with fitted curves and equivalent circuits. (f) LSV curves showing the current densities (j_n) normalized by the ECSA values.

Table 1 The resistance of the electrolyte (R_u), the charge transfer resistance (R_{ct}), the capacitance of the adsorbed OER intermediates (C_a), and the ECSA values of CoFe, CoFeCe$_{0.2}$, CoFeCe$_{0.4}$, CoFeCe$_{0.6}$, and CoFeCe$_{0.8}$

Catalysts	R_u (Ω)	R_{ct} (Ω)	C_a (mF cm^{-2})	ECSA (cm^2)
CoFe	1.17	0.233	101.3	337.7
CoFeCe$_{0.2}$	1.22	0.150	302.3	1007.8
CoFeCe$_{0.4}$	1.24	0.118	300.0	1000.0
CoFeCe$_{0.6}$	1.21	0.157	407.0	1356.8
CoFeCe$_{0.8}$	1.14	0.347	319.4	1064.6

active centers for the OER.[22] Although Ce incorporated CoFeCe$_x$ electrodes exhibit increased ECSAs and greater numbers of active sites, the Ce-based active centers might potentially reduce the intrinsic activity.[12] Therefore, Ce incorporation does not enhance the intrinsic catalytic activity of active sites, and the improved OER performance of CoFeCe$_x$ arises from two synergistic factors, *i.e.*, enhanced charge transfer kinetics at the catalyst–electrolyte interface and increased ECSA.

Stability of electrocatalysts is another vital criterion to evaluate their practical applications. Electrochemical measurements conducted at different times demonstrate the reproduci-
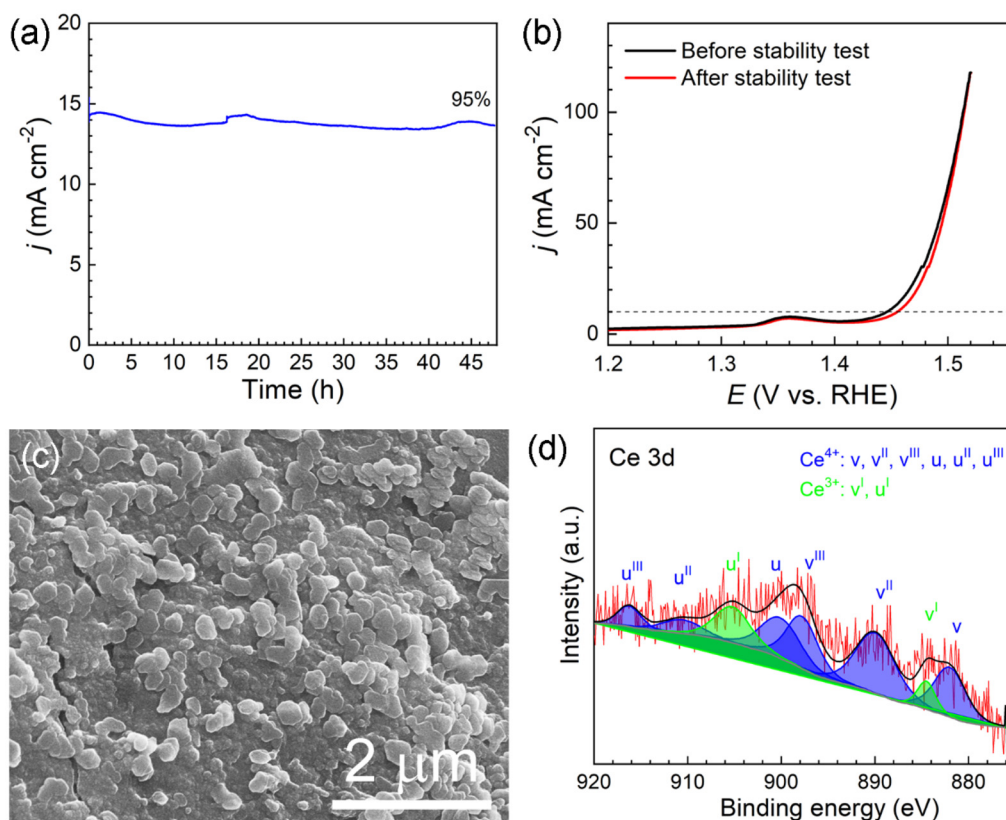
Fig. 5 (a) Chronoamperometric curve of CoFeCe$_{0.4}$ at a potential of 1.47 V for 48 h. (b) LSV curves before and after the stability test. (c) SEM image of CoFeCe$_{0.4}$ after the stability test. (d) Ce 3d XPS spectrum of CoFeCe$_{0.4}$ after the stability test.

bility and reliability of the samples (Fig. S7 and S8). The long-term stability of CoFeCe$_{0.4}$ was evaluated by a chronoamperometric test for 48 h at a fixed potential of 1.47 V (*vs.* RHE). As illustrated by the *i*–*t* curve in Fig. 5a, the current density retains about 95% of its initial value even after 48 h of continuous operation, which demonstrates good durability. The LSV curves before and after the stability test (Fig. 5b) reveal a negligible overpotential shift (∼9 mV) at 10 mA cm^{-2}, confirming the structural stability during the prolonged operation and promising long-term practical application of CoFeCe$_{0.4}$. Furthermore, post-stability characterization studies were performed to analyze the structural changes. The SEM image (Fig. 5c) shows that CoFeCe$_{0.4}$ retains its particle morphology. However, the particle size seems larger after stability testing, likely because small particles corroded during testing. XPS analysis indicated that the Ce content is slightly lower after stability testing, confirming partial Ce dissolution. As evidenced by XPS spectra (Fig. 5d and Fig. S9), Fe, Co, and Ce retain their initial chemical configurations and oxidation states throughout the stability testing, demonstrating the preservation of primary active sites after stability testing, which ensures the excellent stability performance.

Density functional theory (DFT) calculations were carried out to elucidate the electronic structural modulation induced

by Ce incorporation into CoFe (oxy)hydroxide (see the SI for computational details). As shown in Fig. 6a and b, the pristine CoFe (oxy)hydroxide exhibits a band gap (E_g) of 0.39 eV, while the Ce-incorporated structure exhibits a reduced band gap of 0.24 eV, indicating enhanced electronic conductivity.[25,40] The corresponding Density of States (DOS) analysis (Fig. 6c and d) reveals that this improvement mainly arises from a substantial redistribution of Co 3d states induced by Ce doping, characterized by the emergence of additional unoccupied Co 3d orbitals near the Fermi level (E_f), which facilitates electron transfer during the OER.[41–43]

Hirshfeld charge analysis further shows that the average charge on Co atoms increases from 0.18e to 0.26e upon Ce doping, while that on Fe atoms changes by 0.04e, indicating that Ce incorporation predominantly modulates the local electronic environment of Co sites. This observation aligns well with our XPS results. The atomic charge density differences (Fig. S11) further reveal that the introduction of Ce primarily alters the electronic distribution around Co atoms. Moreover, Tafel plots and EIS results demonstrate lower charge transfer resistance in the Ce-doped sample, corroborating the DFT-predicted enhancement in charge transport. These findings collectively highlight the pivotal role of Ce doping in promoting the charge transfer capability of CoFe (oxy)hydroxide.
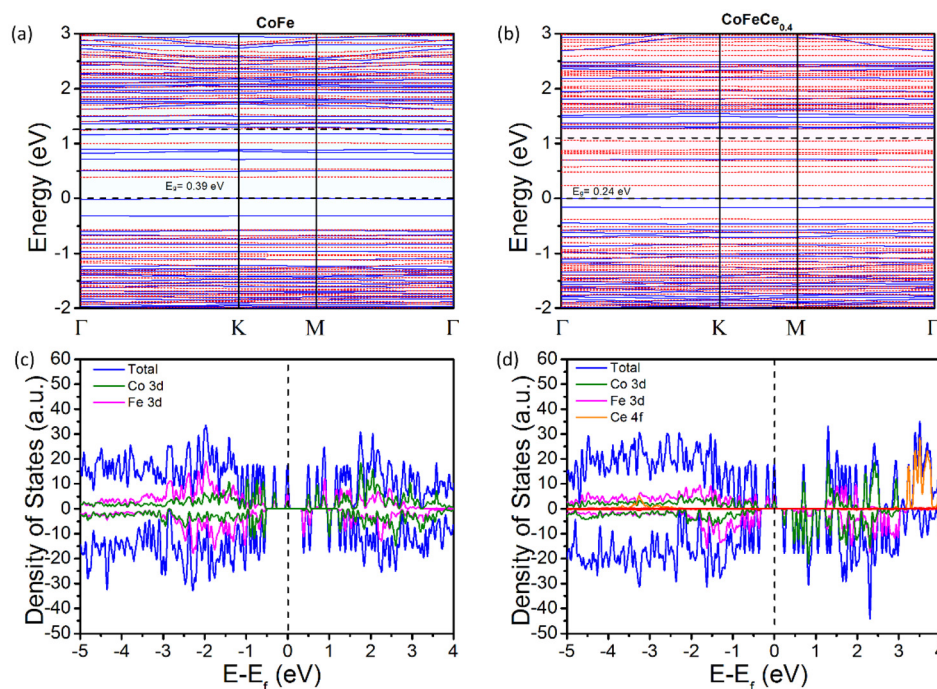
Fig. 6 Band structures of (a) CoFe (oxy)hydroxide and (b) Ce-incorporated CoFe (oxy)hydroxide. Density of states (DOS) of (c) CoFe (oxy)hydroxide and (d) Ce-incorporated CoFe (oxy)hydroxide.

3. Conclusions

In summary, amorphous Ce-incorporated CoFe-(oxy)hydroxide catalysts were synthesized *via* a one-step electrodeposition strategy on NF substrates. The optimized $CoFeCe_{0.4}$ electrode demonstrates excellent OER activity, requiring a low overpotential of 0.220 V to deliver 10 mA cm^{-2}, outperforming most reported CoFe-based catalysts in alkaline media. It is found that Ce incorporation suppresses CoFe particle growth during synthesis, increasing the ECSA by ~3 times. Both experimental and theoretical calculation results demonstrate that Ce incorporation reduces the charge transfer resistance, facilitating the interfacial electron transfer. Although the intrinsic site activity is not improved, the synergistic effect of enhanced ECSA and improved interfacial electron transfer results in the increased OER activity of Ce-incorporated CoFe-(oxy)hydroxides.

Conflicts of interest

There are no conflicts to declare.

Data availability

Necessary datasets supporting this article have been included in the SI. Supplementary information: experimental and computational methods, additional SEM images, EDS spectra, XRD patterns, additional XPS spectra, additional electrochemical results, optimized structures, atomic charge density differ-

ences, and comparison of the OER performance in this work with the recently reported CoFe-based electrocatalysts as well as representative noble metal catalysts. See DOI: **https://doi.org/10.1039/d5dt01962a**.

Additional raw data are available from the corresponding author upon reasonable request.

Acknowledgements

References

1 S. Park, Y. Shao, J. Liu and Y. Wang, *Energy Environ. Sci.*, 2012, **5**, 9331–9344.

2 M. Yang, C. H. Zhang, N. W. Li, D. Luan, L. Yu and X. W. Lou, *Adv. Sci.*, 2022, **9**, 2105135.

3 N. Kittner, F. Lill and D. M. Kammen, *Nat. Energy*, 2017, **2**, 17125.

4 L. C. Seitz, C. F. Dickens, K. Nishio, Y. Hikita, J. Montoya, A. Doyle, C. Kirk, A. Vojvodic, H. Y. Hwang, J. K. Norskov and T. F. Jaramillo, *Science*, 2016, **353**, 1011–1014.

5 H. Over, *Chem. Rev.*, 2012, **112**, 3356–3426.

6 Z. D. Wang, P. T. Liu, C. Y. Yang, Z. H. Zhang, Y. Qian, Y. Q. Zu, X. D. Li and A. L. Feng, *J. Mater. Chem. A*, 2025, **13**, 9974–9982.

7 S. Ghora, R. Chakraborty, S. Bag, M. M. Kumar and C. R. Raj, *Chem. Commun.*, 2025, **61**, 2636–2657.

8 N. T. Suen, S. F. Hung, Q. Quan, N. Zhang, Y. J. Xu and H. M. Chen, *Chem. Soc. Rev.*, 2017, **46**, 337–365.

9 Q. Liu, K. Liu, J. Huang, C. Hui, X. Li and L. Feng, *Dalton Trans.*, 2024, **53**, 3959–3969.

10 Q. Liu, J. Huang, X. Zhang, L. Cao, D. Yang, J. H. Kim and L. Feng, *ACS Sustainable Chem. Eng.*, 2020, **8**, 16091–16096.

11 G. A. Gebreslase, M. V. Martínez-Huerta and M. J. Lázaro, *J. Energy Chem.*, 2022, **67**, 101–137.

12 Z. L. Qing, H. Hu, J. L. Mi, F. M. Qi, J. L. Li, J. D. Song and B. B. Xiao, *ACS Appl. Nano Mater.*, 2024, **7**, 20370–20379.

13 Z. Chen, S. Dong, M. Wang, Z. Hu, H. Chen, Y. Han and D. Yuan, *Inorg. Chem.*, 2023, **62**, 2826–2837.

14 Y. Zhou, J. Hu, L. Yang and Q. Gao, *Chin. Chem. Lett.*, 2022, **33**, 2845–2855.

15 J. Shi, D. Wang, Y. Liang, Q. Xu and Q. Li, *Chem. – Eur. J.*, 2025, **31**, e202404278.

16 Y. Wang, D. Yan, S. E. Hankari, Y. Zou and S. Wang, *Adv. Sci.*, 2018, **5**, 1800064.

17 H. Liu, Y. Wang, X. Lu, Y. Hu, G. Zhu, R. Chen, L. Ma, H. Zhu, Z. Tie, J. Liu and Z. Jin, *Nano Energy*, 2017, **35**, 350–357.

18 A. L. Wang, H. Xu and G. R. Li, *ACS Energy Lett.*, 2016, **1**, 445–453.

19 C. He, J. Zhang, D. Mantzavinos, A. Katsaounis, D. H. Si, Z. Yan, H. Y. Zhang and Z. W. Jiang, *Angew. Chem., Int. Ed.*, 2025, **64**, e202420295.

20 F. Song and X. Hu, *Nat. Commun.*, 2014, **5**, 4477.

21 J. Tang, J. Hu, X. Chen, B. Yang, K. Zhang, Y. Li, Y. Yao and S. Zhang, *Fuel*, 2024, **365**, 131128.

22 L. Wang, Y. Liu, X. Liu and W. Chen, *Dalton Trans.*, 2023, **52**, 12038.

23 Z. Chen, S. Dong, M. Wang, Z. Hu, H. Chen, Y. Han and D. Yuan, *Inorg. Chem.*, 2023, **62**, 2826–2837.

24 S. Anantharaj and S. Noda, *Small*, 2020, **16**, 1905779.

25 M. Li, L. Tao, X. Xiao, X. Jiang, M. Wang and Y. Shen, *ACS Sustainable Chem. Eng.*, 2019, **7**, 4784–4791.

26 Q. Wu, L. Huang, L. Chen, B. Qin and P. Zhang, *J. Appl. Electrochem.*, 2025, **55**, 1415–1428.

27 F. M. Li, X. B. Li, S. Y. Ma, L. Chen, W. Q. Li, C. T. Zhu, X. L. Xu, Y. Chen, Y. F. Li and G. Lawson, *J. Alloys Compd.*, 2015, **649**, 1136–1144.

28 F. M. Qi, W. Xu and J. L. Mi, *ChemCatChem*, 2022, **14**, e202200347.

29 D. Li, B. Zhang, S. Yue, T. Shao, S. Yang, R. Cao and Mi. Cao, *ACS Appl. Nano Mater.*, 2025, **8**, 11114–11123.

30 E. Zhang, B. Wang, X. Yu, J. Zhu, L. Wang and B. Lu, *Energy Storage Mater.*, 2017, **8**, 147–152.

31 B. J. Tan, K. J. Klabunde and P. M. A. Sherwood, *Chem. Mater.*, 1990, **2**, 186–191.

32 N. S. McIntyre and M. G. Cook, *Anal. Chem.*, 1975, **47**, 2208–2213.

33 H. Yan, J. Bai, J. Wang, X. Zhang, B. Wang, Q. Liu and L. Liu, *CrystEngComm*, 2013, **15**, 10007.

34 Y. Pei, Y. Ge, H. Chu, W. Smith, P. Dong, P. M. Ajayan, M. Ye and J. Shen, *Appl. Catal., B*, 2019, **244**, 583–593.

35 L. Kuai, J. Geng, C. Chen, E. Kan, Y. Liu, Q. Wang and B. Geng, *Angew. Chem., Int. Ed.*, 2014, **53**, 7547–7551.

36 F. Dionigi, J. Zhu, Z. Zeng, T. Merzdorf, H. Sarodnik, M. Gliech, L. Pan, W. W. Li, J. Greeley and P. Strasser, *Angew. Chem., Int. Ed.*, 2021, **60**, 14446–14457.

37 S. Watzele and A. S. Bandarenka, *Electroanalysis*, 2016, **28**, 2394–2399.

38 R. D. Smith, C. Pasquini, S. Loos, P. Chernev, K. Klingan, P. Kubella, M. R. Mohammadi, D. Gonzalez-Flores and H. Dau, *Nat. Commun.*, 2017, **8**, 2022.

39 Z. K. Goldsmith, A. K. Harshan, J. B. Gerken, M. Vörös, G. Galli, S. S. Stahl and S. Hammes-Schiffer, *Proc. Natl. Acad. Sci. U. S. A.*, 2017, **114**, 3050–3055.

40 H. Hu, Y. C. Yong, P. Zhang, W. Tang, B. B. Xiao and J. L. Mi, *J. Mater. Chem. A*, 2024, **12**, 2267–2282.

41 W. Cao, X. H. Gao, J. Wu, A. Q. Huang, H. Hu and Z. W. Chen, *ACS Catal.*, 2024, **14**, 3640–3646.

42 L. Y. Xiao, C. Q. Cheng, T. T. Yang, J. T. Zhang, Y. J. Han, C. Y. Han, W. X. Lv, H. T. Tan, X. R. Zhao, P. F. Yin, C. K. Dong, H. Liu, X. W. Du and J. Yang, *Adv. Mater.*, 2024, **36**, 2411134.

43 W. Liu, H. Liu, L. Dang, H. Zhang, X. Wu, B. Yang, Z. Li, X. Zhang, L. Lei and S. Jin, *Adv. Funct. Mater.*, 2017, **27**, 1603904.